Characterization of elastic topological states using dynamic mode decomposition

Shuaifeng Li,[1] Panayotis G. Kevrekidis,[2] and Jinkyu Yang[1,3]
[1]*Department of Aeronautics and Astronautics, University of Washington, Seattle, Washington 98195, USA*
[2]*Department of Mathematics and Statistics, University of Massachusetts, Amherst, Massachusetts 01003, USA*
[3]*Department of Mechanical Engineering, Seoul National University, Seoul 08826, Republic of Korea*

(Received 15 October 2022; accepted 4 May 2023; published 18 May 2023)

Elastic topological states have been receiving increased attention in numerous scientific and engineering fields due to their defect-immune nature, resulting in applications of vibration control and information processing. Here, we present the data-driven discovery of elastic topological states using dynamic mode decomposition (DMD). The DMD spectrum and DMD modes are retrieved from the propagation of the relevant states along the topological boundary, where their nature is learned by DMD. Applications such as classification and synthesis of wave propagation can be achieved by the underlying characteristics from DMD. We demonstrate the classification between topological and traditional metamaterials using DMD modes. Moreover, the model enabled by the DMD modes realizes the synthesis of topological state propagation along the given interface. Our approach to characterizing topological states using DMD can pave the way towards data-driven discovery of topological phenomena in material physics and more broadly lattice systems.

DOI: 10.1103/PhysRevB.107.184308

I. INTRODUCTION

Wave propagation is a typical spatiotemporal phenomenon, which is ubiquitous across science and engineering, especially in fluid dynamics [1,2], geoscience [3,4], plasmas [5], optics [6], atomic and condensed-matter physics [7], as well as the more recent field of metamaterials [8–10]. Topological metamaterials have attracted considerable attention not only because of their theoretical significance but also for practical purposes related to materials applications. Wave propagation in elastic topological metamaterials has prominent applications, such as information transmission and vibration control, due to the topological protection [11–16].

The computations involving the propagation of associated waveforms rely mostly on numerical discretization, e.g., finite-element and discrete-element methods, rather than analytic closed-form solutions which are rarely available in exact form. This naturally generates high-dimensional representations of the solution to accurately reflect the underlying dynamics in both time and space [11,13,14,17]. However, this may occasionally be in contrast with the low-dimensional nature of the underlying dynamics and poses a computational challenge, especially in higher-dimensional settings. In a concurrent study, topological wave propagation has been decomposed into a limited subset of closely spaced modes inside the band gap, possessing nontrivial phase differences. The prediction of group velocity and the application of such a method on a damped system have also been demonstrated [18]. Although the underlying idea of a reduced-order description is similar to that of the present work, still, the data-driven (and possibly model agnostic) analysis and modeling of elastic topological states remain far less explored, in stark contrast with the extensive studies on experimental observation, numerical computation, and theoretical modeling. The data-driven approach can also provide an equation-free and model-agnostic way to reveal the spatiotemporal dynamics and underlying physics purely from data. It is the purpose of the present work to offer a step forward towards filling that void.

Reduced-order models offer representations of the spatiotemporal wave propagation based on the inherently low-rank structure of the simulation data. Within the palette of relevant techniques, dynamic mode decomposition (DMD) is a powerful dimensionality reduction method to create reduced-order models which identifies spatiotemporal coherent structures from high-dimensional data [19]. DMD offers a modal decomposition, where each mode contains spatially correlated structures with the same linear behavior in time, such as oscillations at a certain frequency with growth or decay. Compared with one of the most commonly used dimensionality reduction methods, proper orthogonal decomposition, DMD demonstrates not only dimensionality reduction, but also a reduced model that accounts for how these modes evolve over time. Lately, DMD has been successfully applied to fluid dynamics [19,20], control [21], robotics [22], and biological science [23–25]. Hence, developing such an approach for wave propagation in topological metamaterials is highly desirable.

Here, we develop a data-driven framework using DMD for identifying interpretable low-dimensional representations for wave propagation in elastic topological metamaterials created by a select spring-mass system example. The low-dimensional spatiotemporal coherent structures of topological state propagation in our system are extracted, which correspond to the topological edge states inside the band-gap region. These spatiotemporal coherent structures allow for the qualitative reconstruction of the topological state propagation. Moreover, we first demonstrate how to classify the topological and traditional metamaterials using DMD modes via unsupervised clustering. Furthermore, a portion of the data, referred to as

the training data, is used to synthesize the future evolution of the topological states of interest along a predefined interface with arbitrary shape. Our study provides a computationally tractable data-driven characterization of the relevant states and their propagation, paving the way towards the classification and synthesis of wave propagation in elastic metamaterials.

Our presentation hereafter will be structured as follows. In Sec. II we offer details about the physical system under consideration including the band structure and topological properties. In Sec. III we provide a concise introduction to the mathematical and computational details of the DMD algorithm (including technical modifications to the standard algorithm such as the use of a stacking data matrix leveraged herein) and illustrate how it can be used to represent the wave dynamics. In Sec. IV, we use DMD modes to classify the topological and traditional metamaterials. Finally, in Sec. V, we summarize our findings and provide some directions for future study. The appendixes offer details about further technical aspects of the DMD implementation, such as the DMD spectra, the application of time-delay embedding, and synthesis of topological state propagation.

II. DESIGN OF TOPOLOGICAL ELASTIC METAMATERIALS

To demonstrate DMD on the wave propagation in the topological elastic metamaterials system of interest, we first construct the topological valley metamaterials using a spring-mass system, which is realized by alternating the masses at different sites of the unit cell of the honeycomb lattice [14,17,26,27]. As displayed in Fig. 1(a), the unit cell is composed of two masses m_1 and m_2 connected by a spring. The length and the spring constant are a and k_{spring}. Therefore, the basic vectors for this unit cell are $\vec{a}_1 = [a_x, -a_y]$, $\vec{a}_2 = [a_x, a_y]$, where $a_x = 3a/2$ and $a_y = \sqrt{3}a/2$. The unit cell has four degrees of freedom specified by the displacement of m_1 and m_2 ($U = [u_x^{m_1}, u_y^{m_1}, u_x^{m_2}, u_y^{m_2}]^T$). After applying the periodic boundary condition to the unit cell (Bloch's theorem), equations of motion of two masses in one unit cell can be written as

$$\begin{aligned} -\omega^2 m_1 \vec{u}^{(1)} &= k_{\text{spring}}\left[\left(\vec{u}^{(2)} - \vec{u}^{(1)}\right)\cdot \vec{e}_x\right]\vec{e}_x \\ &+ k_{\text{spring}}\left[\left(\vec{u}^{(2)} e^{i\vec{k}\cdot\vec{a}_1} - \vec{u}^{(1)}\right)\cdot \vec{e}_k\right]\vec{e}_k \\ &+ k_{\text{spring}}\left[\left(\vec{u}^{(2)} e^{i\vec{k}\cdot\vec{a}_2} - \vec{u}^{(1)}\right)\cdot \vec{e}'_k\right]\vec{e}'_k, \end{aligned} \tag{1}$$

$$\begin{aligned} -\omega^2 m_2 \vec{u}^{(2)} &= k_{\text{spring}}\left[\left(\vec{u}^{(1)} - \vec{u}^{(2)}\right)\cdot \vec{e}_x\right]\vec{e}_x \\ &+ k_{\text{spring}}\left[\left(\vec{u}^{(1)} e^{-i\vec{k}\cdot\vec{a}_1} - \vec{u}^{(2)}\right)\cdot \vec{e}_k\right]\vec{e}_k \\ &+ k_{\text{spring}}\left[\left(\vec{u}^{(1)} e^{-i\vec{k}\cdot\vec{a}_2} - \vec{u}^{(2)}\right)\cdot \vec{e}'_k\right]\vec{e}'_k, \end{aligned} \tag{2}$$

where $\vec{e}_x = [1,\ 0]^T$, $\vec{e}_k = [-\frac{1}{2}, \frac{\sqrt{3}}{2}]^T$, and $\vec{e}'_k = [-\frac{1}{2}, -\frac{\sqrt{3}}{2}]^T$ are three unit vectors along the springs on one mass. The band structure $\omega(k)$ of our system can be obtained by solving the eigenvalue equation as a function of Bloch wave vector k in the first Brillouin zone.

$$[D(k) + \omega^2 M]U = 0. \tag{3}$$

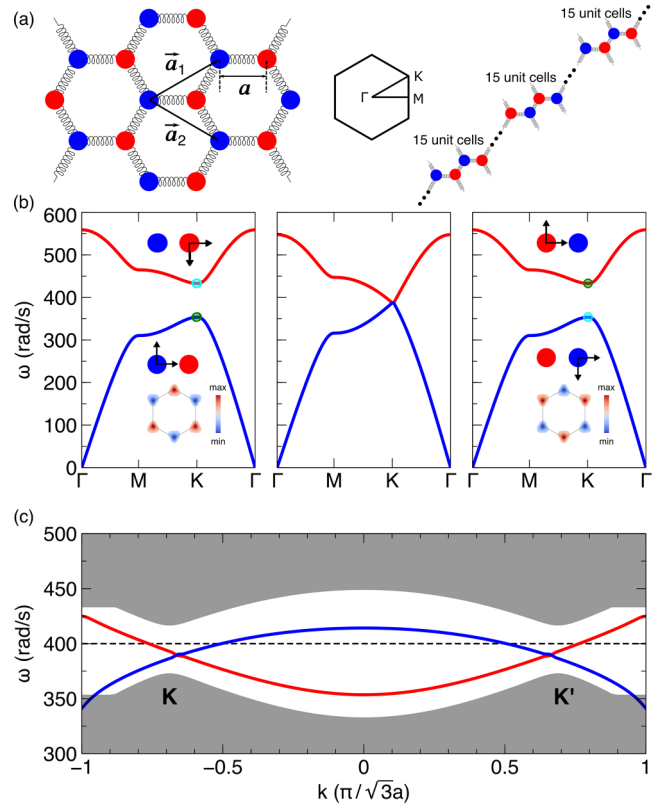

FIG. 1. Band structure of the valley topological metamaterials. (a) Schematic of our elastic metamaterials based on the spring-mass system. Basic vectors of unit cell are shown in $\vec{a}_1$ and $\vec{a}_2$. Length of the spring is a. First Brillouin zone with high-symmetry points Γ, M, and K is shown in the middle panel. Sandwiched supercell for the calculation of projected band structure is shown in the right panel. (b) Band structure when (left) $m_1 = 0.8$ kg, $m_2 = 1.2$ kg, (middle) $m_1 = 1$ kg, $m_2 = 1$ kg, and (right) $m_1 = 1.2$ kg, $m_2 = 0.8$ kg are shown. Eigenmodes corresponding to the K valley are shown in the first panel and the third panel. Motions along horizontal and vertical directions are marked on the two sites. Berry curvatures around the valley of the first band for each case are shown in the inset. (c) Projected band structure with two topological states inside the band gap. Black dashed line indicates the excitation frequency of the simulation setup.

Here, ω denotes the angular frequency of the propagating wave, M is the mass matrix, and $D(k)$ is the stiffness matrix as a function of Bloch wave vector k. The corresponding eigenmodes $U = [u_x^{m_1}, u_y^{m_1}, u_x^{m_2}, u_y^{m_2}]^T$ can also be obtained.

As for our specific system, we choose the equal masses on two sites ($m_1 = m_2 = 1$ kg) and $k_{\text{spring}} = 10^5$ N/m to find the Dirac point at the corner of the Brillouin zone (K point), as shown in the middle panel of Fig. 1(a). After breaking spatial inversion symmetry by unequal masses on two sites, two bands can be opened to form a band gap. The left and right panels exhibit the band structure when $m_1 = 0.8$ kg, $m_2 = 1.2$ kg, and $m_1 = 1.2$ kg, $m_2 = 0.8$ kg, respectively. At the K valley, eigenmodes corresponding to two bands when $m_1 = 0.8$ kg and $m_2 = 1.2$ kg are $U_1 = \frac{1}{\sqrt{2}}[0, 0, 1, -i]^T$ and $U_2 = \frac{1}{\sqrt{2}}[1, i, 0, 0]^T$, while the eigenmodes are $U_1 = \frac{1}{\sqrt{2}}[1, i, 0, 0]^T$ and $U_2 = \frac{1}{\sqrt{2}}[0, 0, 1, -i]^T$ after alternating the masses on two

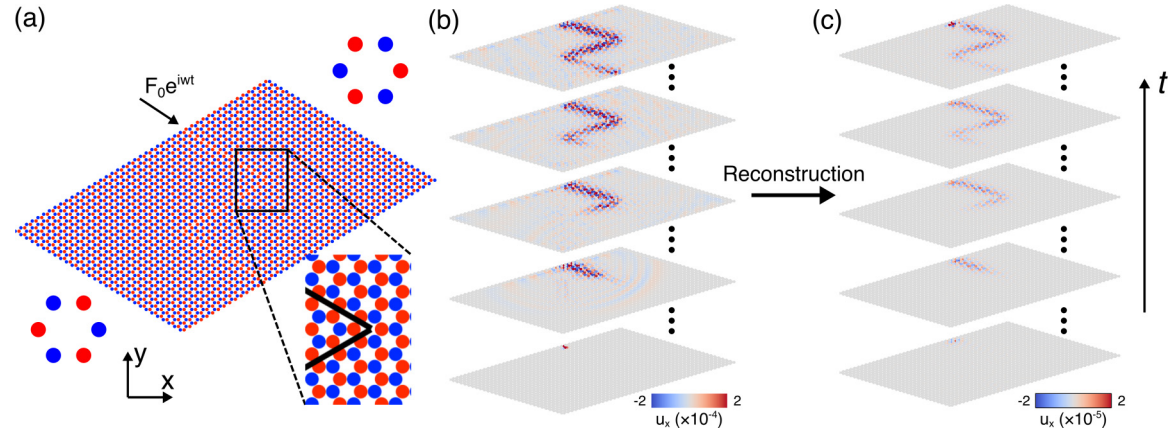

FIG. 2. Setup for simulation and for the numerical DMD implementation. (a) Simulation of wave propagation along the *Z*-shaped interface in a valley topological metamaterial built by means of a spring-mass system. Two different unit cells with two different topological phases are shown on the two sides. Magnified view of the topological boundary (black line) is shown in the inset. (b), (c) Snapshots of original and reconstructed wave propagation represented by the horizontal displacement u_x along the *Z*-shaped interface at $t = 2$, 192, 380, 570, and 758 ms (with the time evolving from the bottom to the top), respectively.

sites (see the insets with black arrows that represent the eigenmodes). The obvious band inversion can be seen from the eigenmodes of the unit cell.

To further confirm the band inversion in this process, the topological properties of our topological valley system are also explored to show the topological phase transition. After obtaining the band structure $\omega(k)$ and the corresponding eigenmode $U(k)$, we calculate the Berry curvature $\Omega(k) = i\nabla_k \times \langle u(k)|\nabla_k|u(k)\rangle$ using a numerical discretization method (in momentum space) [11,12]. For our two-dimensional system, the Brillouin zone is discretized to numerous small patches centered at $A(k_x,\ k_y)$ with vertices $A_1(k_x - \delta k_x/2,\ k_y - \delta k_y/2)$, $A_2(k_x - \delta k_x/2,\ k_y + \delta k_y/2)$, $A_3(k_x + \delta k_x/2,\ k_y + \delta k_y/2)$, and $A_4(k_x + \delta k_x/2,\ k_y - \delta k_y/2)$, where the Berry curvature for each small patch can be expressed as

$$\Omega(A) = \frac{\mathrm{Im}[\langle U(A_1) \mid U(A_2)\rangle + \langle U(A_2) \mid U(A_3)\rangle + \langle U(A_3) \mid U(A_4)\rangle + \langle U(A_4) \mid U(A_1)\rangle]}{\delta k_x \times \delta k_y}. \tag{4}$$

As shown in the inset of Fig. 1(b), the nonzero Berry curvatures are distributed near the corners of the Brillouin zone (*K* points) and different valleys possess opposite Berry curvatures. Due to our system with time-reversal symmetry, the integration of the Berry curvature around the whole Brillouin zone is expected to be zero. However, the local integration around the valleys of the Berry curvature converges to nonzero quantized value, which is referred to as valley Chern number $C_v = \frac{1}{2\pi}\int_v \Omega(k)d^2k$, representing the valley topology. The obvious inversion of Berry curvature distribution and the sign of the valley Chern number after alternating the masses on two sites clearly shows the topological phase transition [compare the insets of the right and left panels in Fig. 1(b)].

The projected band structure is then calculated using a sandwiched supercell shown in the right panel of Fig. 1(a). The sandwiched supercell combines the metamaterials of three arrangements: (i) $m_1 = 0.8$ kg and $m_2 = 1.2$ kg, (ii) $m_1 = 1.2$ kg and $m_2 = 0.8$ kg, and (iii) $m_1 = 0.8$ kg and $m_2 = 1.2$ kg, which has two opposite Berry curvature distributions in the Brillouin zone. When two systems are interfaced with opposite Berry curvature, the bulk-boundary correspondence principle ensures that two topological states with different pseudospins corresponding to two types of interfaces emerge inside the band gap, as shown in Fig. 1(c). The bulk features by *K* and *K*' valleys can also be observed from the projected band structure. In the following study, the excitation frequency of our simulation is 400 rad/s as indicated by the black dashed line in Fig. 1(c).

III. CHARACTERIZATION BY DYNAMIC MODE DECOMPOSITION

As shown in Fig. 2(a), our system bears a *Z*-shaped interface which is formed by combining metamaterials with two opposite topological phases. In Fig. 2(a), one such interface is formed by $m_1 = 0.8$ kg (blue) and $m_2 = 1.2$ kg (red) shown in the bottom, while the other is formed by $m_1 = 1.2$ kg (red) and $m_2 = 0.8$ kg (blue) shown in the top, i.e., with the masses flipped. The spring constant is fixed to be 10^5 N/m. As analyzed in the previous section, with such a configuration, the topological states will emerge along the interface formed by two metamaterials.

The system is excited by an oscillating force with the angular frequency of 400 rad/s at the input port of the *Z*-shaped interface shown in Fig. 2(a). The masses at the boundaries of the system are connected to springs fixed to the wall, i.e., $\vec{F}_{\mathrm{boundary}} = -k_{\mathrm{spring}}\vec{u}$, where $\vec{u}$ contains horizontal displacement u_x and vertical displacement u_y. Because of the

topological protection of wave propagation, the elastic wave can travel through the sharp bend robustly, the horizontal displacement u_x of which is visualized as the time-series snapshots in Fig. 2(b).

Next, we attempt to reconstruct this wave propagation phenomenon using the DMD approach. Let us present the result of the DMD approach first. Figure 2(c) shows the reconstruction of the horizontal displacement u_x. We find the trend of the DMD-based approach is similar to the one by the original evolution dynamics. Particularly, the DMD technique successfully captures the robust propagation of topological waves around the sharp corners, which is the signature characteristic of the topological waveguide. The difference of the color intensity between the original and the reconstructed results is due to inherent deficiency of the DMD to capture transient dynamics which will be elaborated later.

As introduced in Sec. I, DMD serves as the dimensionality reduction method to generate a low-dimensional model. The basic idea of DMD is to find a matrix representation A to relate two matrices X and X'. In our case, two data matrices are constructed for standard DMD by stacking the horizontal displacement u_x and vertical displacement u_y as follows, resulting in two $2n \times (m-1)$ matrices, where n is the number of masses and m is the number of used snapshots over time ($n = 2700$ and $m = 379$ for Z-shaped interface based on the numerical simulations of 758 ms duration with 2 ms time interval):

$$X = \begin{bmatrix} | & | & & | \\ x_1 & x_2 & \cdots & x_{m-1} \\ | & | & & | \end{bmatrix} \quad X' = \begin{bmatrix} | & | & & | \\ x_2 & x_3 & \cdots & x_m \\ | & | & & | \end{bmatrix}, \tag{5}$$

where $\begin{bmatrix} | \\ x_m \\ | \end{bmatrix} = \begin{bmatrix} | \\ u_{xm} \\ | \\ u_{ym} \\ | \end{bmatrix}$ for simplicity of description. X and X' may be related by a best-fit linear operator A that minimizes the Frobenius norm error $\|X' - AX\|_F$ given by

$$X' = AX \Rightarrow A = X'X^{\dagger}, \tag{6}$$

where $X^{\dagger}$ is the Moore-Penrose pseudoinverse [28]. Because $2n \gg m$ for our systems, instead of obtaining A directly, we seek the eigendecomposition of A. After X is decomposed using singular value decomposition (SVD) and the proper rank-r truncation is chosen so that $\tilde{X} = \tilde{U}\tilde{\Sigma}\tilde{V}^T$, where $\tilde{U} \in \mathbb{R}^{2n\times r}$, $\tilde{\Sigma} \in \mathbb{R}^{r\times r}$ and $\tilde{V} \in \mathbb{R}^{(m-1)\times r}$ are the left unitary matrix, diagonal matrix with singular values, and right unitary matrix, respectively, the matrix representation $\tilde{A}$ can be written as

$$\tilde{A} = \tilde{U}^* X' \tilde{V} \tilde{\Sigma}^{-1}, \tag{7}$$

where the $*$ denotes the conjugate transpose. The eigendecomposition of $\tilde{A}$ results in the matrix of eigenvectors W and eigenvalues λ, which are the DMD eigenvalues. This further derives the corresponding DMD mode ϕ, which is the column of $\Phi = X'\tilde{V}\tilde{\Sigma}^{-1}W$.

As discussed in Appendix A, the rank-r truncation is chosen to be $r = 131$ to minimize the reconstruction error and also to eliminate the noise in the simulation data. Each DMD mode ϕ corresponds to an eigenvalue λ. The temporal dynamics, referring to growth/decay and the frequency of oscillation of each DMD mode ϕ, is reflected through the magnitude and phase of eigenvalue λ, respectively. In our case, because the raw data are strictly real valued, the decomposition yields complex conjugate pairs of eigenvalues and modes.

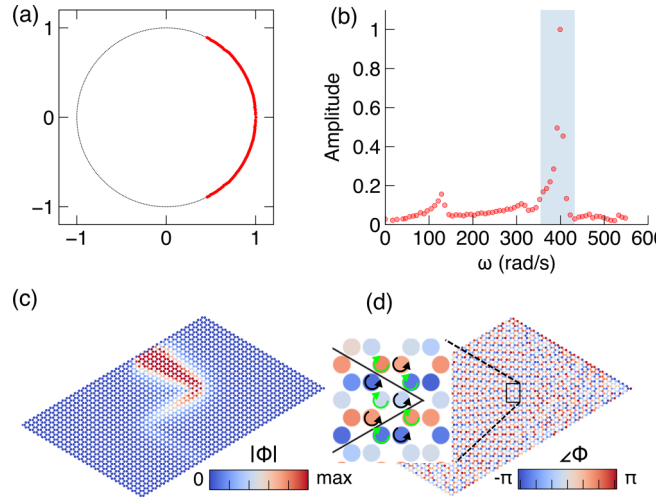

FIG. 3. DMD spectrum and DMD modes. (a) Eigenvalues are visualized on the complex plane located around the unit circle. (b) Mode amplitude varies as a function of frequency. Shading area indicates the band-gap region. (c) Magnitude of the DMD mode with the largest amplitude inside the band-gap region. (d) Phase of the DMD mode with the largest amplitude inside the band-gap region. Inset shows the magnified view around the interface (black line) illustrating the phase difference and valley pseudospin. Black and green arrows show the pseudospin up and pseudospin down indicated by the phase evolution around hexagon corners, respectively.

In Fig. 3(a), the eigenvalues λ are visualized on the unit circle in the complex plane, suggesting the corresponding modes are oscillating with certain frequencies. The frequencies are defined as $\omega = |\text{imag}(\frac{\log\lambda}{\Delta t})|$ and the mode amplitudes are defined as $P = |\phi|_2^2$, which is the squared ℓ^2 norm of the DMD modes. Figure 3(b) gives the DMD spectrum which provides specific spatial modes in our system for different frequencies. It is obvious that there is a region with large mode amplitudes corresponding to the band-gap region (shaded area). The mode with the largest amplitude inside the band-gap region is chosen as the prototypical mode used to visualize the motion of our system. The horizontal displacement u_x is chosen for the description below. Note that there are two small peaks outside the band-gap region due to the resonance of the masses at the boundary, corresponding to the resonant frequencies $\omega = \sqrt{\frac{7-\sqrt{33}}{4}}\omega_0$ and $\omega = \sqrt{\frac{1}{2}}\omega_0$ approximated by a simple model that one mass is connected to two walls and two masses on nearest honeycomb corners by springs.

Figure 3(c) exhibits the magnitude of this most dominant DMD mode of our system, also showcasing the interface-involving dynamics. The decaying magnitude from the input along the Z-shaped interface is due to the constant force excitation at the input. The characteristics of interface states present concentrated displacement along the Z-shaped interface and rapid decay away from the interface. Moreover, the DMD modes showcase the fact that the elastic wave can travel

along an interface featuring bends. Apart from the magnitude, the phases of the DMD mode also reflect the important characteristics of our topological valley metamaterials, as shown in Fig. 3(d). The distribution of phase along the interface has a certain alignment, where the magnified view around the interface clearly shows the phase difference around the corners of the honeycomb, indicating specific valley polarization along a certain topological interface. The counterclockwise and clockwise phase evolutions are shown on three corners and the other three corners of the honeycomb, suggesting the valley pseudospin of the excited valley in our system. The valley pseudospin here refers to the phase difference of DMD modes around the corners of honeycomb. Note that the other DMD modes inside the band gap have a similar pattern and it is these modes that will be primarily used to reconstruct the dynamical evolution below.

The DMD spectra of wave propagation in topological metamaterials with a straight interface and a cross-shaped interface will be further illustrated in Appendix B. Similarities between the DMD spectra and modes can be found in topological state propagation along different interfaces including the high amplitude inside the band gap and the topological interface states reflected by the DMD modes. This demonstrates the ability of the DMD to robustly show the frequency spectrum of the system purely from the data and to discover the nature of topological state propagation.

Using the extracted DMD modes and corresponding time dynamics, we can reconstruct the wave propagation in topological metamaterials using the following expression:

$$\hat{X} = \Phi \Lambda^{t-1} Z, \tag{8}$$

where the diagonal entries of Λ contain DMD eigenvalues and $Z = \Phi \backslash x_1$. x_1 is the initial condition of our system and backslash is to solve the linear system following the MATLAB notation. Here, we only use the DMD modes inside the band-gap region (10 pairs of DMD modes) and the corresponding eigenvalues to reconstruct the whole process of wave propagation, as displayed in Fig. 2(c) with several time-series snapshots representing the wave propagation in our system. Similar patterns can be found compared with the original snapshots of wave propagation.

In Fig. 4, we quantify the reconstruction error as a function of duration (black line) calculated by $E(t) = \frac{|X(t)-\hat{X}(t)|_2}{|X(t)|_2}$, where $|\cdot|_2$ represents ℓ^2 norm that is the square root of the sum of the absolute squares of the vector entries. Most relative errors are around 0.97 and oscillating over time. This nontrivial relative error may result from the reduction of inessential modes with extremely small singular values by the SVD, the significant reduction of DMD modes when considering solely modes within the band gap, the ℓ^2-norm error requiring the high accuracy of displacement for every mass, and, most importantly, the inherent deficiency of the DMD method to capture transient phenomena [23,29,30]. This is caused by the fact that temporal dynamics cannot be well approximated by $e^{\omega t}$ where the imaginary number $\omega = \frac{\ln \Lambda}{\Delta t}$. The SVD-based method also performs poorly on handling translational symmetry of the wave propagation due to the coupling between time and space. Although the relative error is rather nontrivial, the wave propagation along the Z-shaped interface can be clearly observed from Fig. 1(c) and Supplemental Material [31], which can be considered as the qualitative representation of the original wave propagation. To measure the qualitative reconstruction using DMD, we propose an additional quantity, namely the correlation coefficient, to show the similarity between reconstructed and original wave propagation at each time point:

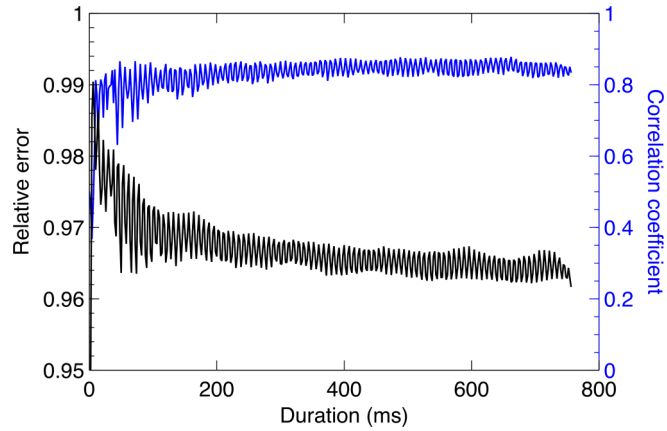

FIG. 4. Reconstruction error and correlation coefficient between reconstructed and original wave propagation. Relative error and correlation coefficient between the ground truth and reconstruction as a function of duration are shown in black and blue, respectively.

$$r(t) = \frac{\sum_{i=1}^{2n} (x_{i,t} - \bar{x}_{*,t})(\hat{x}_{i,t} - \hat{x}_{*,t})}{\sqrt{\sum_{i=1}^{2n} (x_{i,t} - \bar{x}_{*,t})^2} \sqrt{\sum_{i=1}^{2n} (\hat{x}_{i,t} - \hat{x}_{*,t})^2}}, \tag{9}$$

where the hat indicates the reconstructed data and the bar indicates the mean. The correlation coefficient as a function of time shown in blue line in Fig. 4 is over 0.8, suggesting the high similarity between reconstructed and original wave propagation. Therefore, the DMD reconstruction using the modes inside the band-gap region qualitatively captures the evolution dynamics despite the substantially reduced dimensionality of the system.

DMD can accurately capture the frequency range and characteristics of topological states of elastic topological metamaterials. The nature of the valley pseudospin in our valley system can also be revealed, suggesting that DMD, functioning as a data-driven method, is able to learn the topological nature. In stark contrast with the original transient displacement data, the DMD spatial mode can explicitly show the topological nature. In addition, the propagation of topological states can be reconstructed qualitatively only by the DMD modes inside the band gap and the corresponding time dynamics. The additional study in Appendix C is carried out on the topological metamaterial excited by a transient force, which further demonstrates the ability of DMD to qualitatively reconstruct the dynamics under different forms of excitations. Note that we use standard DMD based on SVD in the main text, but another variant, DMD with time-delay embedding, has demonstrated the ability of increasing the accuracy of reconstruction in several applications [23,24,32–34]. In Appendix D and the associated figure, we also show the partial decrease of reconstruction error using the augmented data matrix formed by shift stacking the original data matrix.

IV. CLASSIFICATION OF TOPOLOGICAL AND TRADITIONAL METAMATERIALS

Compared with the topological metamaterials, traditional metamaterials function by defect states that cannot support robust transport of elastic waves [35–38]. By using the transient displacement data, it is difficult to classify the topological and traditional metamaterials using simple classification methods because of the high-dimensional nature. Here, we demonstrate how to use the extracted DMD modes from topological and traditional metamaterials to classify them. The topological metamaterial is in the aforementioned configuration and the traditional metamaterial is constructed based on the defect states by the metamaterial with $m_1 = 0.8$ kg and $m_2 = 1.2$ kg, where the masses are replaced by $m_2 = 1.2$ kg along the Z-shaped interface to create defects. Because of the defect state, the traditional metamaterial serves as a waveguide similar to the topological metamaterial but without the topological protection.

The original DMD modes are high dimensional and thus difficult to classify using a classification algorithm directly. Therefore, the feasible way is to find a feature space to project the DMD modes on, resulting in a low-dimensional representation. Specifically, we construct a library of DMD modes inside the band gap from topological metamaterials and traditional metamaterials L:

$$L = \begin{bmatrix} | & | & & | \\ \phi_1 & \phi_2 & \cdots & \phi_N \\ | & | & & | \end{bmatrix}. \tag{10}$$

For the purpose of classification, we consider the absolute value of every element of normalized DMD modes and denote the resulting matrix as $|L|$. To simplify this problem, clusters are determined in one-dimensional principal component space, using the projections of each column of $|L|$ onto the proper principal components of $|L|$:

$$|L| = U_L \Sigma_L V_L^*. \tag{11}$$

with this expression yielding the SVD of the matrix $|L|$ and using

$$P = U_i^T |L| = \Sigma_i V_i^T, \tag{12}$$

where U_i^T, Σ_i, and V_i^T are the transpose of the ith column of U_L, ith singular value, and the transpose of the ith column of V_L, respectively. Note that the transpose of V_L is the same as the conjugate transpose of V_L due to the real value.

The principal components can explain a significant proportion of the variance in the features in topological and traditional metamaterials. Therefore, finding a proper principal component U_i^T is key to distinguish two types of metamaterials. Also, the proper principal component is physically interpretable to contain the features differentiating two types of metamaterials. After examining all principal components, we have found that the second principal component is a suitable feature towards the classification task at hand (classification results are the same as the labeled dataset). The second principal component of $|L|$ is shown in Fig. 5(a) [see the second principal components of $|L|$ for straight and cross interfaces shown in Fig. 10(a) and Fig. 10(b) in Appendix E]. The reason why the second principal component is optimally suited to serve as the feature space is that this pattern of the

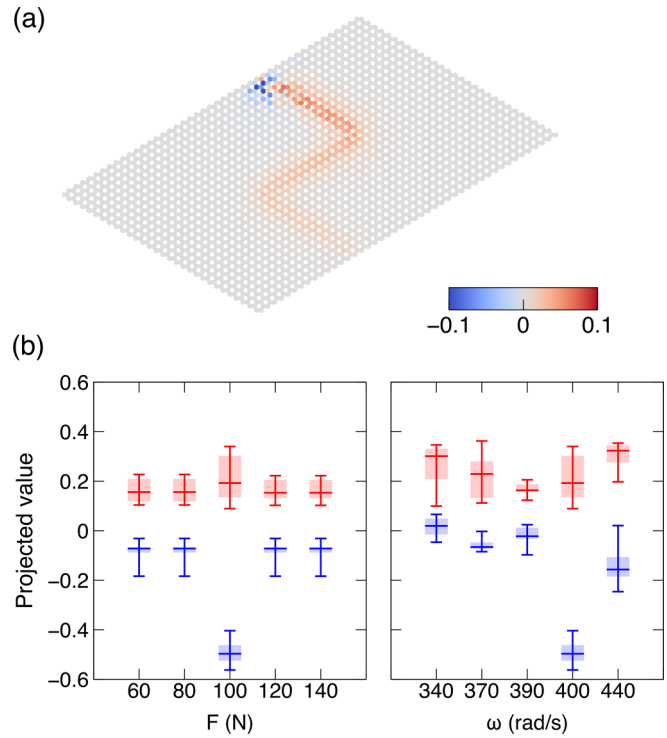

FIG. 5. Classification of topological and traditional metamaterials. (a) Feature space formed by the second principal component of DMD modes with Z-shaped interface. (b) Projected values of each DMD mode from the topological and traditional metamaterials excited by different forces (left panel) and different excitation frequencies (right panel). Red and blue regions indicate topological and traditional DMD modes, respectively. Error bars indicate the range of the minima and maxima of projected values.

principal component shows the difference between topological and traditional metamaterials at the beginning of the input port (positive vs negative values, respectively). We find that it corresponds to the distinction of backscattering in topological and traditional metamaterials. In the traditional metamaterial, due to the interference of elastic waves traveling in opposite directions, elastic waves experience strong backscattering when encountering bends, obstacles, or even traveling along the straight interface. Therefore, when $|L|$ is projected onto this principal component, the two types of metamaterials can be classified whereas they cannot be classified when $|L|$ is projected onto other principal components. The relevant diagnostic allows us to distinguish topological and traditional metamaterials purely from the wave propagation phenomena represented by the displacement, corresponding to topologically protected wave propagation and nontopological wave propagation, and hence, accordingly classify them. Note that from the perspective of the underlying topological physics, the topological invariants of the bulk and the bulk-edge correspondence are principles used to classify topological and traditional systems.

Then, in order to test whether this feature space can be generalized to classify topological and traditional systems, we apply the feature space (of the second principal component) obtained above to the topological and traditional metamaterials under the excitation of different forces F_0 and

different angular frequencies ω_0. As shown in Fig. 5(b), it is obvious that the projected values for topological and traditional metamaterials under the excitation of different forces can be separated well and can be simply classified using the k-means unsupervised clustering [39]. Likewise, under the excitation of different frequencies, the projected values for topological and traditional metamaterials are separated well, leading to good classification results. Using the same method, the wave propagation along different interfaces (straight and cross interfaces) in topological and traditional metamaterials under the excitation of different forces and frequencies can also be classified, as detailed in Appendix E. The classification results for straight and cross interfaces are demonstrated in the relevant figure therein. The case for the straight interface indicates that elastic waves in the traditional metamaterial experience backscattering without the bend because of the interference of guided waves propagating to opposite directions. The classification results and ground truth have excellent agreement. The DMD modes with improved accuracy calculated by DMD with time-delay embedding (Appendix D) can also be used in the classification, resulting in better separation of topological and traditional metamaterials in the feature space. It should be expected that with the decrease of the Berry curvature in the topological metamaterials induced by the decrease in degree of broken-inversion symmetry, the classification of two types of metamaterials would become progressively more difficult. This is because the intervalley scattering becomes larger in the topological metamaterials, resulting in the similar wave propagation in topological and traditional metamaterials [12,16].

V. CONCLUSIONS AND FUTURE CHALLENGES

In this paper, we provide a guide towards the potential impacts of the application of the DMD method on the wave propagation in topological elastic metamaterials. The analysis of DMD eigenvalues and spectrum shows the oscillation and frequency of the DMD modes. The notable topological interface states and valley pseudospin of the valley system can be reflected by the DMD modes. Furthermore, the reconstruction of topological state propagation is achieved by the low-dimensional model constructed only by the DMD modes inside the band gap and the corresponding time dynamics. Apart from the fundamental characterization by DMD, we demonstrate the potential that the method bears as concerns the tasks of classification and synthesis of wave propagation along the given interface using DMD modes and associated reduced dynamical descriptions (Appendix F). We find a feature space with particular characteristics to project the DMD modes on for the classification of topological and traditional metamaterials. The synthesis of wave propagation along the given interface can be achieved by the extension and shift of DMD modes, where the ℓ^2-norm error and correlation coefficient are at an acceptable level to visualize the future wave propagation. The DMD provides a data-driven method to explore the wave propagation in topological metamaterials and to reveal the potential topological nature, filling an important research void at the interface of the corresponding fields. It also opens up an avenue to classify and synthesize the wave propagation through a purely data-driven approach.

Naturally, this is only a first step along this direction and raises several questions that still merit further addressing. One key aspect of interest concerns how to reduce the error and overcome the inherent deficiency of DMD. While the results presented herein represent adequate reconstructions (and even synthetic wave propagation along the given interface) of the time-evolution dynamics, it would be highly desirable for such examples to match far more adequately, in a quantitative sense, the real system dynamics. From the point of view of applications, it would be relevant to explore the method in other classes of systems including in ones stemming from higher dimensions and to explore how adequately the method can fare in such more data-intensive settings. Additionally, the characterization of the topological metamaterials with different Berry curvatures by DMD can be conducted through the same process. Similar results, such as DMD spectrum, modes, and low-dimensional model, are expected but classification between two types of metamaterials can be less efficient as discussed in Sec. IV. Such topics are presently under consideration and associated potential progress will be reported in future publications.

ACKNOWLEDGMENTS

The present paper is based on work that was supported by the U.S. National Science Foundation under Grants No.

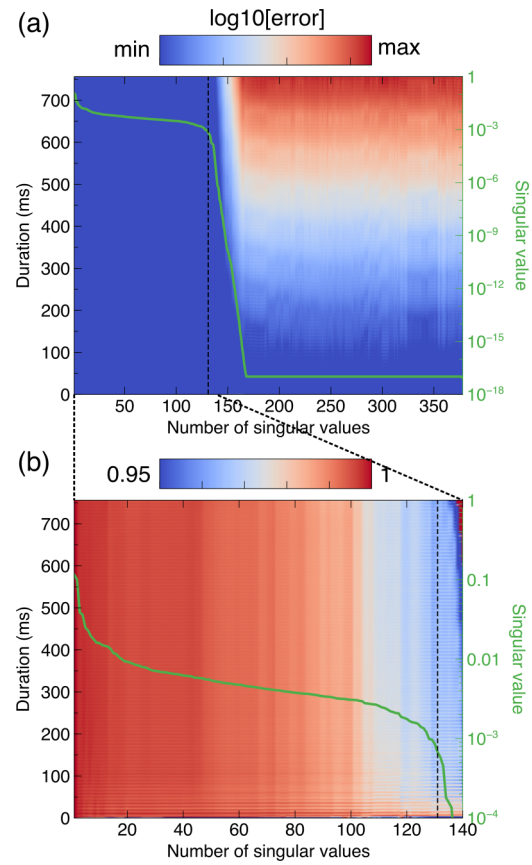

FIG. 6. (a) Reconstruction error as a function of truncation and duration. Error is shown on a logarithmic scale. (b) Zoom-in reconstruction error as a function of truncation from 1 to 140 and duration. Vertical dashed lines in (a) and (b) correspond to the selected $r = 131$.

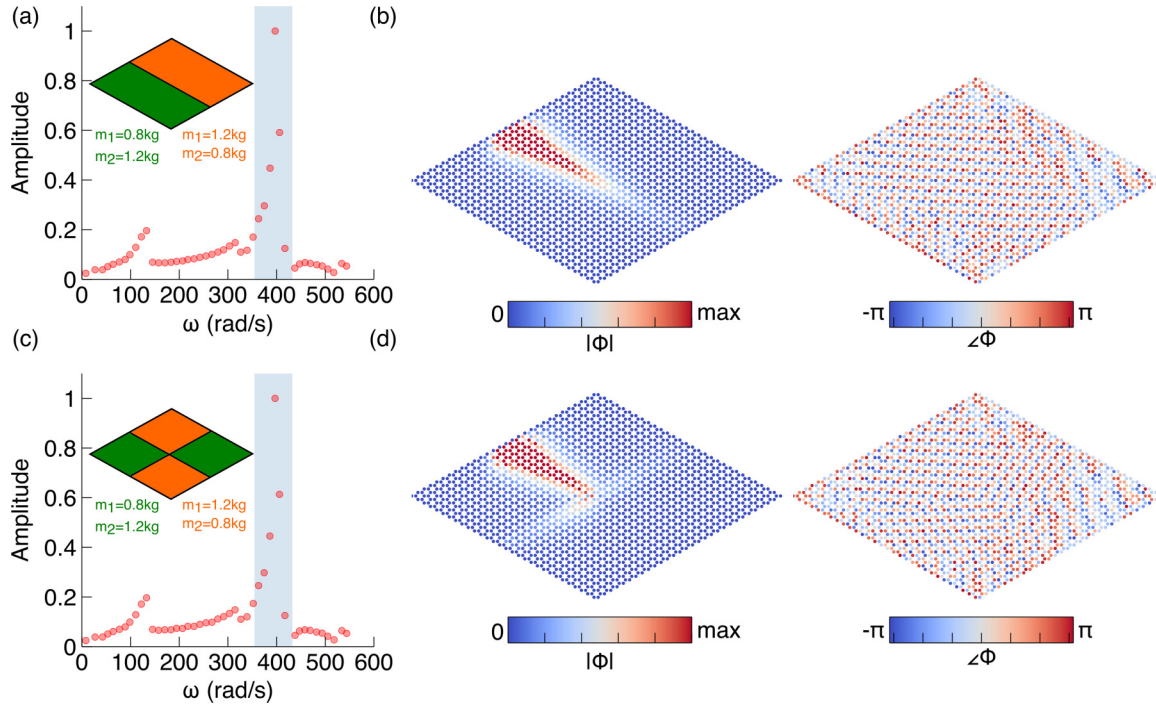

FIG. 7. DMD spectrum and DMD modes of straight interface and cross interface are shown in (a), (b) and (c), (d), respectively. Insets in (a) and (c) are the configurations of elastic topological metamaterials.

EFRI-1741685 (S.L. and J.Y.), No. DMS-1809074 (P.G.K.), and No. DMS-2204702 (P.G.K.). J.Y. also acknowledges the support from SNU-IAMD, SNU-IOER, and National Research Foundation grants funded by the Korea government [Grants No. 2023R1A2C2003705 and No. 2022H1D3A2A03096579 (Brain Pool Plus by the Ministry of Science and ICT)].

APPENDIX A: THE TRUNCATION OF SINGULAR VALUES OF THE DATA MATRIX

Choosing the proper truncation of the singular value decomposition of X is important to obtain the best-fit linear operator A. To identify the truncation r of the singular values, we wish to ensure the minimization of the reconstruction error. The reconstruction $\hat{X}$ is conducted by DMD modes inside the band-gap region and corresponding time dynamics and is compared with the original wave propagation. In Fig. 6(a), the map of the reconstruction error calculated by $E(t) = \frac{|X(t)-\hat{X}(t)|_2}{|X(t)|_2}$ is given as a function of the number of singular values (truncation r) and duration. The singular value spectrum shows that singular values decay slowly, indicating that many modes are needed. Accordingly, with the increase of the number of singular values in a certain range ($1 \sim 140$), the reconstruction error does not change significantly in the logarithm scale. However, when the number of singular values further increases, the reconstruction error will significantly increase.

Therefore, the proper truncation is in the range of 1 to 140, which we magnify in Fig. 6(b). As the number of singular values increases, the reconstruction error will decrease to a minimum. We choose the $r = 131$ as the number of singular values corresponding to the inflection point in the singular value spectrum.

APPENDIX B: DMD SPECTRA AND MODES OF WAVE PROPAGATION ALONG INTERFACE WITH DIFFERENT SHAPES

Figure 7(a) gives the DMD spectrum indicating the relation between the frequency and the mode amplitude for the topological states propagation along the straight interface (configuration shown in the inset). Similar to Fig. 2(b), it is clear that the region with high mode amplitude corresponds to the band-gap region (shaded area). The mode inside the band-gap region with the largest amplitude is chosen as the prototypical mode of interest (and of relevance to the dynamics). Figure 7(b) exhibits the magnitude and phase of this dynamic spatial mode of our system. The interface state can be observed from the magnitude of the DMD modes. The displacement is concentrated along the straight interface and decays rapidly away from the interface. The elastic waves can travel along the interface with bends. The phases of the DMD modes also reflect the characteristics of topological states. The distribution of phase along the interface has a certain pattern, representing the valley pseudospin of our system as described in the main text. Likewise, in Figs. 7(c) and 7(d), we calculate the DMD spectrum and DMD modes inside the band-gap region with the largest amplitude for the topological states propagation along the cross interface (configuration shown in the inset). The DMD mode in Fig. 7(d) shows that the elastic wave travels along the path at the beginning and when it arrives at the intersection, it propagates to two sides instead of the straight path. Because of the valley-locking effect, the

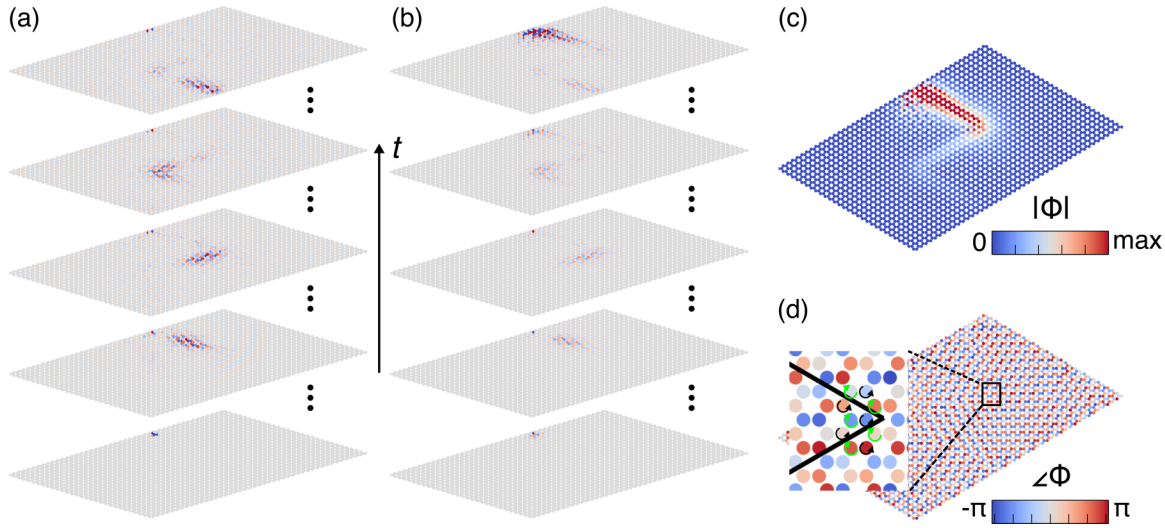

FIG. 8. DMD implementation. (a), (b) Snapshots of original and reconstructed wave propagation excited by the Gaussian burst represented by the horizontal displacement u_x along a Z-shaped interface at $t = 2$, 192, 380, 570, and 758 ms (with the time evolving from the bottom to the top), respectively. (c) Magnitude of the DMD mode with the largest amplitude inside the band-gap region. (d) Phase of the DMD mode with the largest amplitude inside the band-gap region. Inset shows the magnified view around the interface (black line) illustrating the phase difference and valley pseudospin. Black and green arrows show the pseudospin up and pseudospin down indicated by the phase evolution around hexagon corners, respectively.

wave will propagate along certain interface with same valley projection [11,40–42]. The generated elastic wave is projected by the K valley according to the group velocity in projected band structure [Fig. 1(c)]. Therefore, the elastic wave will only propagate along the K-valley projected topological interfaces. Note that apart from DMD modes shown in Fig. 7(b) and Fig. 7(d) which have the largest amplitudes in the DMD spectra, other DMD modes inside the band-gap region are also interface states.

APPENDIX C: DMD IMPLEMENTATION ON THE TOPOLOGICAL STATE PROPAGATION EXCITED BY A TRANSIENT SOURCE

In the main text, our system with Z-shaped interface is excited by a constant harmonic force. Now, we explore the system excited by a transient source. In our example, we use the Gaussian tone burst $F = F_0 e^{-(\frac{\omega t}{30})^2}\cos(\omega t)$ to excite our system and follow the procedure introduced in the main text to analyze the system's response using DMD. Figure 8(a) shows several snapshots of wave propagation along the Z-d interface; we can observe that an elastic wave can propagate through the shape bend smoothly due to the topological protection. Figure 8(b) exhibits the reconstructed wave propagation by DMD reconstruction, which is visually similar to the original evolution dynamics although it starts to blow up at the input port at the end of the reported time horizon, suggesting the qualitative nature of the reconstruction. Similar to the situation in the main text, Fig. 8(c) exhibits the magnitude of DMD modes showing that an elastic wave can travel along an interface featuring bends. As shown in Fig. 8(d), the phase of the DMD mode indicates the phase difference around the corners of the honeycomb and the valley pseudospin of the excited valley in our system. This demonstrates the ability of DMD to learn the topological nature of the wave propagation in topological metamaterials.

APPENDIX D: DYNAMIC MODE DECOMPOSITION WITH TIME-DELAY EMBEDDING

Recently, the approach of time-delay embedding has been shown to be a general method to generate proper observable measurements to render the reconstruction more accurate as discussed in the main text. By embedding future temporally consecutive snapshots into the current snapshot, time-delay embedding augments the limited spatial observables and provides extra observables. The DMD with time-delaying embedding can be achieved by the augmented data matrix X_{aug} by shift stacking the original data matrix as shown below:

$$X_{\text{aug}} = \begin{bmatrix} | & | & & | \\ x_1 & x_2 & \cdots & x_{m-h} \\ | & | & & | \\ | & | & & | \\ x_2 & x_3 & \cdots & x_{m-h+1} \\ | & | & & | \\ | & | & & | \\ x_h & x_{h+1} & \cdots & x_{m-1} \\ | & | & & | \end{bmatrix}, \tag{D1}$$

where h is the number of stacks. X'_{aug} can be induced likewise. Using the augmented data matrix to conduct DMD, the reconstruction error can be reduced. As shown in Fig. 9, the relative error calculated by $E = \frac{|X-\hat{X}|_F}{|X|_F}$ decreases with the increase of the number of stacks and becomes saturated at around 0.65 even with a larger number of stacks. The error may come from the inherent deficiency of DMD on the wave propagation problem as discussed in Sec. III. However, when the number of stacks increases, the augmented data matrix becomes large,

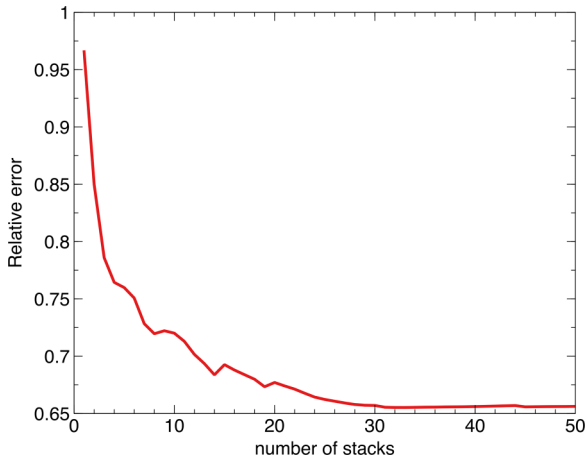

FIG. 9. Relative error of reconstruction as a function of number of stacks.

leading to a heavy computation cost. Therefore, there is a tradeoff balance between accuracy and efficiency in the case of real-world applications and practitioners should seek to strike a relevant balance to that effect.

APPENDIX E: CLASSIFICATION OF TOPOLOGICAL AND TRADITIONAL METAMATERIALS WITH DIFFERENT INTERFACES

For classification of topological and traditional metamaterials with different interfaces, we follow the method we introduce in the main text. The topological metamaterial is composed of the metamaterial with $m_1 = 0.8$ kg and $m_2 = 1.2$ kg and the metamaterial with $m_1 = 1.2$ kg and $m_2 = 0.8$ kg. The traditional metamaterial is constructed based on the defect states by the metamaterial with $m_1 = 0.8$ kg and $m_2 = 1.2$ kg, where the masses are replaced by $m_2 = 1.2$ kg along the straight and cross interface to create defects. Following the method in the main text, we extract the principal components of the library composed of DMD modes of topological and traditional metamaterials with different interfaces (straight and cross interfaces). As for different shapes of the interfaces, the feature space from the principal components for the DMD modes to project on can be determined as visualized in Figs. 10(a) and 10(c), corresponding to the straight interface and cross interface. Similarly, the feature spaces are also the second principal components in the SVD, in which the main difference between topological wave propagation and nontopological wave propagation is reflected, and hence can classify two types of metamaterials. We test the feature space on the case excited under different forces and different frequencies. After the DMD modes inside the band gap for both topological and traditional metamaterials are projected onto the feature space, the DMD modes lead to a scalar value, which is separated well between the two families, and can be classified using the k-means unsupervised clustering, as shown in Figs. 10(b) and 10(d). For both wave propagation along straight interface and cross interface, the classification results and ground truth have excellent agreement.

APPENDIX F: SYNTHETIC WAVE PROPAGATION ALONG THE GIVEN INTERFACE USING DMD

We demonstrate another application of the usefulness of DMD modes in topological metamaterials. Synthetic wave

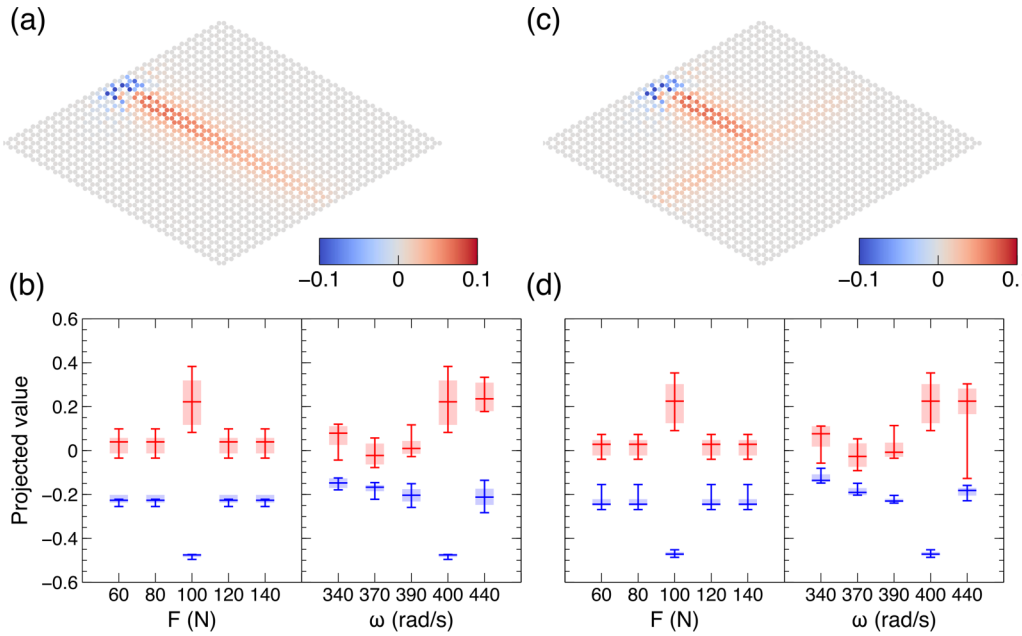

FIG. 10. Classification of topological and traditional waveguides with different interface. (a), (c) Feature space of topological metamaterials with straight interface and cross interface. (b), (d) Projected values of each DMD mode extracted from the system under excitation of different forces and different frequencies, corresponding to straight interface (a) and cross interface (c). Red and blue regions indicate topological and traditional DMD modes, respectively. Error bars indicate the range of the minima and maxima of projected values.

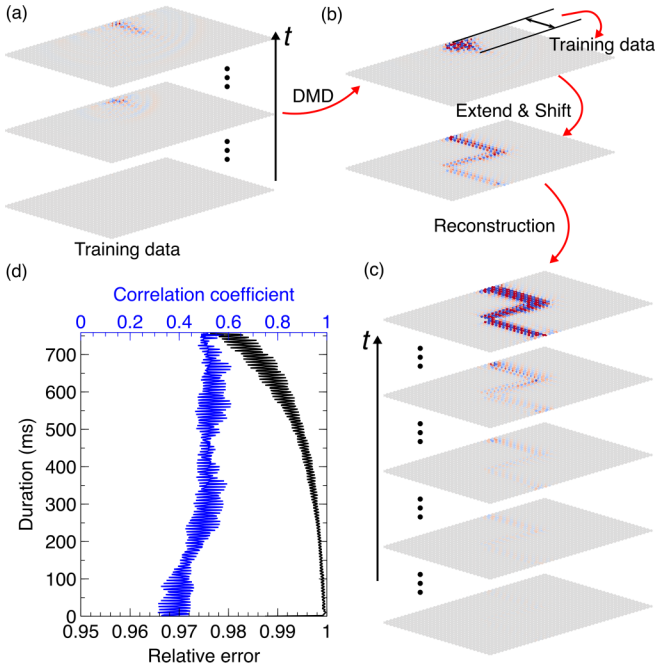

FIG. 11. Synthesis of topological states propagation along the given interface. (a) Snapshots of horizontal displacement u_x from 0 to 200 ms used for training. (b) Top panel displays one of the DMD modes inside the band gap of the training data. Bottom panel displays the corresponding extended and shifted DMD modes along the *Z*-shaped interface. (c) Snapshots of the horizontal displacement u_x for the synthetic wave propagation at $t = 2$, 192, 380, 570, and 758 ms. (d) Synthesis error and correlation coefficient as a function of duration are shown in black line and blue line, respectively.

propagation along the given interface is important when there is lack of data due to the sensor problems or measurement difficulties. DMD is capable of extracting the time dynamics and corresponding dynamic modes, which can help with the synthetic topological state propagation along the given interface. Here, we use DMD modes calculated from a part of data (training data) to build a low-dimensional model, and with the knowledge of the position of interface further to synthesize the future propagation of elastic wave. Here, as shown in Fig. 11(a), we use the wave propagation in topological metamaterials from 0 to 200 ms as the training data. Then, DMD is used to extract the DMD modes inside the band gap and the corresponding time dynamics (two pairs of DMD modes inside the band gap are used). Since wave propagation is a process with time and space variation together, the DMD modes are limited in space due to the nature of spatial modes, resulting in stoppage of the wave and, accordingly, failure of the synthesis. A feasible way that we have found relevant towards bypassing this issue is to extend the DMD modes along the (*a priori*) given interface and to approximate the future wave propagation using the extended DMD modes and the time dynamics from the training data.

First, the least-squares method is used in order to identify the time-varying wave velocity $\vec{c}(t)$ by a set of pairs of the positions of wave front and corresponding time. Therefore, the position of wave front can be determined at arbitrary time. Next, after the extracted DMD modes inside the band gap are reshaped to a matrix form, they are truncated based on the displacement $d = \int_0^t c(t')dt'$, corresponding to the number of matrix columns, as shown in the training data in Fig. 11(b). The DMD is used again to predict the DMD modes in the future when the elastic wave propagates to the arbitrary position. The synthesis time is determined by the length of the given interface. Note that extension by DMD only considers the speed of wave propagation, assuming that it is effectively constant during each segment of the interface, instead of other associated properties such as the dispersive radiation, which is found to be minimal in the present setting. Then, the extended DMD modes ϕ_e are shifted according to the shape of the interface, resulting in the shifted DMD mode ϕ_s. As an example, one of the DMD modes inside the band gap is shown in Fig. 11(b), where the DMD mode is constrained in space which will cause the stoppage of wave propagation after 200 ms. After being extended by DMD and shifted by the shape of interface, the DMD mode constrained in a certain space can cover the given interface (*Z*-shaped interface), as shown in Fig. 11(b). Finally, after we extend and shift all DMD modes inside the band gap from the training data, the time dynamics of the training data are used to synthesize the wave propagation along the *Z*-shaped interface, detailed as below:

$$\hat{X} = \Phi_s \Lambda^{t-1} Z_s, \tag{F1}$$

where Φ_s is formed by ϕ_s. The diagonal entries of Λ contain DMD eigenvalues from training data and $Z_s = \Phi_s \backslash x_1$. x_1 is the initial condition of our system. As shown in Fig. 11(c), several snapshots of synthetic wave propagation clearly exhibit the elastic wave traveling along the *Z*-shaped interface. This process is qualitatively similar to the snapshots shown in Fig. 2(b). According to Fig. 11(d), the relative error compared with the reconstructed results in Fig. 2(b) is in the range of $0.95 \sim 1$. Likewise, we use the correlation coefficient to characterize the qualitative performance of reconstruction, which is around 0.5. This is smaller than that for the reconstruction due to the limited number of modes and time dynamics. Yet, this synthesis of wave propagation along the given interface still provides a reasonable visualization of future wave propagation. It should be mentioned that aforementioned approach of DMD with time-delay embedding can also be used in the synthesis since this approach can generate the dynamics and corresponding modes.

[1] E. Infeld and G. Rowlands, *Nonlinear Waves, Solitons and Chaos* (Cambridge University Press, Cambridge, 2000).

[2] M. J. Ablowitz, *Nonlinear Dispersive Waves: Asymptotic Analysis and Solitons* (Cambridge University Press, Cambridge, 2011).

[3] C. Chapman, *Fundamentals of Seismic Wave Propagation* (Cambridge University Press, Cambridge, 2004).

[4] B. Poursartip, A. Fathi, and J. L. Tassoulas, Large-scale simulation of seismic wave motion: A review, Soil Dyn. Earthq. Eng. **129**, 105909 (2020).

[5] M. Kono and M. Skoric, *Nonlinear Physics of Plasmas* (Springer, Berlin, Heidelberg, 2010).

[6] Y. S. Kivshar and G. P. Agrawal, *Optical Solitons: From Fibers to Photonic Crystals* (Academic Press, San Diego, 2003).

[7] L. Pitaevskii and S. Stringari, *Bose-Einstein Condensation and Superfluidity* (Oxford University Press, Oxford, 2016).

[8] E. Kim and J. Yang, Review: Wave propagation in granular metamaterials, Funct. Compos. Struct. **1**, 012002 (2019).

[9] J. Liu, H. Guo, and T. Wang, A review of acoustic metamaterials and phononic crystals, Crystals **10**, 305 (2020).

[10] M. A. Butt, S. N. Khonina, and N. L. Kazanskiy, Recent advances in photonic crystal optical devices: A review, Opt. Laser Technol. **142**, 107265 (2021).

[11] S. Li and J. Yang, Topological Transition in Spiral Elastic Valley Metamaterials, Phys. Rev. Appl. **15**, 014058 (2021).

[12] S. Li, I. Kim, S. Iwamoto, J. Zang, and J. Yang, Valley anisotropy in elastic metamaterials, Phys. Rev. B **100**, 195102 (2019).

[13] S. Li, D. Zhao, H. Niu, X. Zhu, and J. Zang, Observation of elastic topological states in soft materials, Nat. Commun. **9**, 1370 (2018).

[14] H. Chen, H. Nassar, and G. L. Huang, A study of topological effects in 1D and 2D mechanical lattices, J. Mech. Phys. Solids **117**, 22 (2018).

[15] T. W. Liu and F. Semperlotti, Tunable Acoustic Valley-Hall Edge States in Reconfigurable Phononic Elastic Waveguides, Phys. Rev. Appl. **9**, 014001 (2018).

[16] H. Zhu, T. W. Liu, and F. Semperlotti, Design and experimental observation of valley-Hall edge states in diatomic-graphene-like elastic waveguides, Phys. Rev. B **97**, 174301 (2018).

[17] Y. Zhou, P. R. Bandaru, and D. F. Sievenpiper, Quantum-spin-Hall topological insulator in a spring-mass system, New J. Phys. **20**, 123011 (2018).

[18] J. R. Tempelman, A. F. Vakakis, and K. H. Matlack, A modal decomposition approach to topological wave propagation, arXiv:2210.11665.

[19] P. J. Schmid, Dynamic mode decomposition of numerical and experimental data, J. Fluid Mech. **656**, 5 (2010).

[20] C. W. Rowley, I. Mezi, S. Bagheri, P. Schlatter, and D. S. Henningson, Spectral analysis of nonlinear flows, J. Fluid Mech. **641**, 115 (2009).

[21] J. L. Proctor, S. L. Brunton, and J. N. Kutz, Dynamic mode decomposition with control, SIAM J. Appl. Dyn. Syst. **15**, 142 (2016).

[22] E. Berger, M. Sastuba, D. Vogt, B. Jung, and H. Ben Amor, Estimation of perturbations in robotic behavior using dynamic mode decomposition, Adv. Robot. **29**, 331 (2015).

[23] B. W. Brunton, L. A. Johnson, J. G. Ojemann, and J. N. Kutz, Extracting spatial-temporal coherent patterns in large-scale neural recordings using dynamic mode decomposition, J. Neurosci. Methods **258**, 1 (2016).

[24] Y. Shiraishi, Y. Kawahara, O. Yamashita, R. Fukuma, S. Yamamoto, Y. Saitoh, H. Kishima, and T. Yanagisawa, Neural decoding of electrocorticographic signals using dynamic mode decomposition, J. Neural Eng. **17**, 036009 (2020).

[25] S. Li, L. M. Roger, J. Klein-Seetharaman, L. J. Cowen, N. A. Lewinski, and J. Yang, Data-driven discovery of spatiotemporal coherent patterns in pulsating soft coral tentacle motion with dynamic mode decomposition, Phys. Rev. Res. **5**, 013175 (2023).

[26] Y. Chen, X. Liu, and G. Hu, Topological phase transition in mechanical honeycomb lattice, J. Mech. Phys. Solids **122**, 54 (2019).

[27] T. Kariyado and Y. Hatsugai, Manipulation of dirac cones in mechanical graphene, Sci. Rep. **5**, 18107 (2016).

[28] R. Penrose, A generalized inverse for matrices, Math. Proc. Cambridge Philos. Soc. **51**, 406 (1955).

[29] J. H. Tu, C. W. Rowley, D. M. Luchtenburg, S. L. Brunton, and J. N. Kutz, On dynamic mode decomposition: Theory and applications, J. Comput. Dyn. **1**, 391 (2014).

[30] A. Mendible, S. L. Brunton, A. Y. Aravkin, W. Lowrie, and J. N. Kutz, Dimensionality reduction and reduced-order modeling for traveling wave physics, Theor. Comput. Fluid Dyn. **34**, 385 (2020).

[31] See Supplemental Material at http://link.aps.org/supplemental/10.1103/PhysRevB.107.184308 for the comparison between original and reconstructed elastic topological state propagation.

[32] P. J. Schmid, Dynamic mode decomposition and its variants, Annu. Rev. Fluid Mech. **54**, 225 (2021).

[33] M. Kamb, E. Kaiser, S. L. Brunton, and J. N. Kutz, Time-delay observables for Koopman: Theory and applications, SIAM J. Appl. Dyn. Syst. **19**, 886 (2020).

[34] Y. Yuan, K. Zhou, W. Zhou, X. Wen, and Y. Liu, Flow prediction using dynamic mode decomposition with time-delay embedding based on local measurement, Phys. Fluids **33**, 095109 (2021).

[35] A. Khelif, A. Choujaa, S. Benchabane, B. Djafari-Rouhani, and V. Laude, Guiding and bending of acoustic waves in highly confined phononic crystal waveguides, Appl. Phys. Lett. **84**, 4400 (2004).

[36] C. He, X. Ni, H. Ge, X. C. Sun, Y. Bin Chen, M. H. Lu, X. P. Liu, and Y. F. Chen, Acoustic topological insulator and robust one-way sound transport, Nat. Phys. **12**, 1124 (2016).

[37] H. Niu, S. Li, and J. Zang, Reliable and tunable elastic interface states in soft metamaterials, Phys. Status Solidi - Rapid Res. Lett. **14**, 2000338 (2020).

[38] H. Niu, S. Li, and J. Zang, Interface-dependent tunable elastic interface states in soft metamaterials, J. Appl. Phys. **129**, 065305 (2021).

[39] S. P. Lloyd, Least squares quantization in PCM, IEEE Trans. Inf. Theory **28**, 129 (1982).

[40] X. Wu, Y. Meng, J. Tian, Y. Huang, H. Xiang, D. Han, and W. Wen, Direct observation of valley-polarized topological edge states in designer surface plasmon crystals, Nat. Commun. **8**, 1304 (2017).

[41] J. Q. Wang, Z. D. Zhang, S. Y. Yu, H. Ge, K. F. Liu, T. Wu, X. C. Sun, L. Liu, H. Y. Chen, C. He, M. H. Lu, and Y. F. Chen, Extended topological valley-locked surface acoustic waves, Nat. Commun. **13**, 1324 (2022).

[42] J. Jiao, T. Chen, and D. Yu, Observation of topological valley waveguide transport of elastic waves in snowflake plates, Compos. Struct. **286**, 115297 (2022).